Vector Scattering Analysis of TPF Coronagraph Pupil Masks

Daniel Peter Ceperley

Electrical Engineering and Computer Sciences
University of California at Berkeley

December 19, 2005

Vector Scattering Analysis of TPF Coronagraph Pupil Masks

by Daniel P. Ceperley

Research Project

Submitted to the Department of Electrical Engineering and Computer Sciences, University of California at Berkeley, in partial satisfaction of the requirements for the degree of **Master of Science, Plan II**.

Approval for the Report and Comprehensive Examination:

Committee:

Professor Andrew R. Neureuther
Research Advisor

Date

* * * * * *

Professor Jeffrey Bokor
Second Reader

Date

Abstract

The finite-difference time-domain (FDTD) method is used to simulate the scattering from prototypical pupil mask cross-section geometries in 2D for the Terrestrial Planet Finder Coronagraph (TPF-C) and to quantify the differences from the normally assumed ideal on-off behavior. Physical effects (such as real metals, thick masks, sidewall geometry, and polarization) are considered along with numerical effects (such as numerical dispersion and source haze) of the FDTD method. The physical studies have shown that undercut angle and mask material are the two most important design choices when moving a shaped pupil mask from theory to implementation.

The accuracy in magnitude and phase required for modeling a chronograph system to achieve the 10^{10} star-light rejection level over the 500-800nm wavelength range is extremely demanding and previously inconsequential numerical errors may be of the same order of magnitude as the physical phenomena under study. Using a cell density of 53cells/wavelength reduces the numerical dispersion to 0.04% and results in PML reflections and source haze three order of magnitude in intensity smaller than the physical effects under study. Effects of thick masks, real materials, and various cross-section geometries on the transmission of pupil-plane masks are illustrated. The differences between the designed opening widths and the electromagnetic widths are examined at the reference plane of the mask opening. Undercutting the edge shape of Cr masks improves the effective opening width to within $\lambda/5$ of the actual opening but, for metals in general, TE and TM polarizations require opposite compensations. Undercutting and doping (or coating with a thin layer of metal) Silicon reduces the difference between the designed and effective opening widths from multiple wavelengths down to less than $\lambda/10$.

Acknowledgments

Table of Contents

List of Figures

List of Tables

Chapter 1

INTRODUCTION

The Terrestrial Planet Finder Coronagraph (TPF-C) is a space-based telescope being designed to detect exo-planets (planets orbiting other stars). A number of space-based telescopes have been designed and built providing a useful foundation on which this telescope can be designed; however, the TPF-C has more extreme requirements than any other telescope designed to date requiring much more extensive modeling than before. The main issue is how to resolve a planet that is 10^{10} times dimmer than the star it is orbiting when the two are only separated by at most 60 milli-arc-seconds. If a simple telescope is created and the starlight is allowed to reach the image plane the planet signal will be hidden by the star. To combat this problem a number of novel techniques have been developed to remove the star's light from the image. One of the most promising technologies is shaped pupil-plane diffraction masks[1]. This technology places metal masks in the telescope's pupil planes to diffract the star-light out of certain parts of the image, leaving planet discovery zones in which a planet's signal will stand out above the background noise floor. In theory, this concept works well; however, a number of simplifications are built into the model that hide potential show-stopping physical phenomena, such as sidewall interactions and polarization dependent opening sizes. These phenomena have been extensively investigated through numerical simulation at Berkeley and this work is the subject of this report.

A recent paper[2] highlights the simulation work and results obtained over the past year and half at Berkeley and in this report we summarize the key findings to provide a reference for the other groups involved in this project. Most of the work discussed herein was performed by the author; however, where

indicated, other peoples' work (most notably that of Ta-Ming Shih, an undergraduate member of the research group) has been included for completeness.

This report starts with background material explaining the TPF-C mission and the simulation methods used in this specific research. This is followed by numerical experiments to explore sources of stray-light and their analyses. Future work focusing on edge generated stray-light sources will appear in [3].

Chapter 2

BACKGROUND

A basic schematic of the TPF-C system is shown in fig. 2.1. The star and planet light enters the telescope at the upper left, reflects off a number of mirrors, and eventually travels down to the image plane CCD while on the way passing through diffraction masks and a deformable mirror.
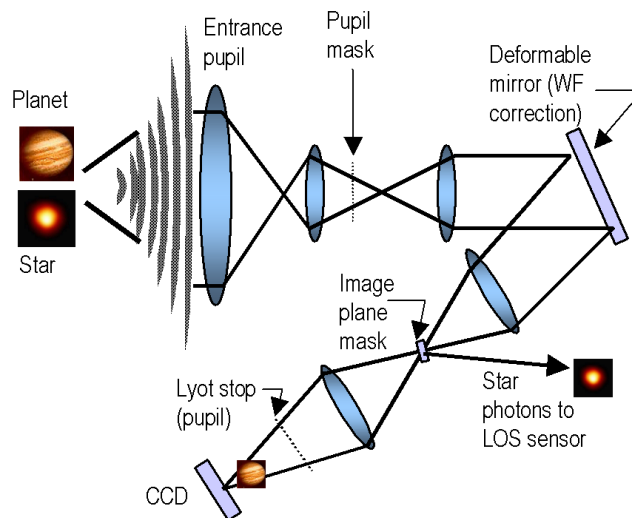
Figure 2.1: Coronagraph optical layout that can accommodate pupil, image, and hybrid mask architectures[4].

As mentioned before, the system is under design and, for the purposes of this work, currently exists as a simulation, the Integrated Telescope Model (ITM),

written by Ball Aerospace and Technologies Corp. It uses Fresnel propagators to move the light from surface to surface and it models the light as a scalar field. The diffraction masks, an example of which is shown in Fig. 2.2, are designed by a group at Princeton University[1]. There are many design tradeoffs to consider

(a) Layout of Spergel pupil mask.

(b) Image from pupil mask showing star and orbiting planet.
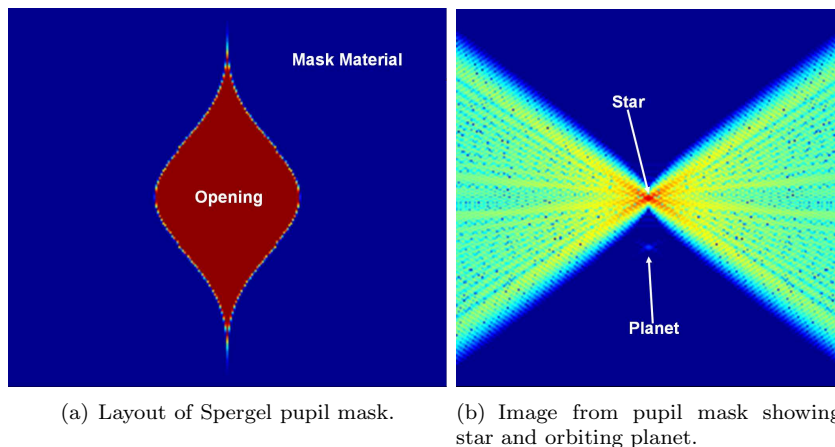
Figure 2.2: A proposed pupil mask for the TPF-C is shown on the left and on the right is the corresponding image of the star and its orbiting planet. Note that the planet is much dimmer than the star so that only the bright central peak of the planet's PSF (Point-Spread Function) is visible [4].

when creating and implementing a mask and different tradeoffs lead to different mask designs. The work presented in this report is based on the Barcode mask (Fig. 2.3). From a numerical simulation standpoint, this mask is advantageous due to its predominately one dimensional design.

Even though this work focuses on the Barcode mask the problems it attempts to solve are common to all mask designs. Specifically, the masks are designed using a number of approximations:

1. The mask is infinitely thin,

2. The mask material is perfectly absorbing,

3. Simple scalar Fraunhofer diffraction can account for all the mask's effects.

There are a number of physical effects taking place on these diffraction masks that are not captured by this simple model. These physical effects can throw light in unexpected places, masking the planet signal. The list of problem areas includes:
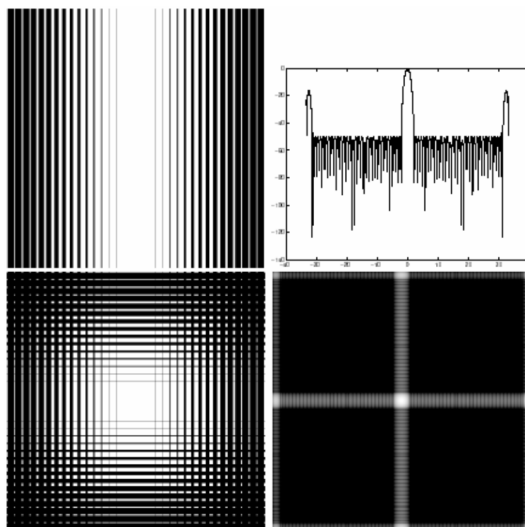
Figure 2.3: The Barcode mask used in these studies. Clockwise from upper left: single mask pattern, cut-line through PSF of single mask, PSF of dual mask configuration (dark quadrants provide 10^{-10} level of starlight suppression), dual mask pattern [5].

1. Real materials - leakage and surface plasmons,

2. Thick masks - sidewall reflections,

3. Sidewall geometry - reflections and glowing corners,

4. Polarization - mask openings have different effective areas depending on polarization.

All of these problems manifest themselves as primarily edge-based phenomena. Away from the edges, the masks reflect or transmit light in a nearly ideal fashion - the mask material acts as a smooth, uniform layer when reflecting light and large mask openings pass light with little effect. Only near the edges do we find light interacting with the sidewalls and corners of the mask producing stray-light. Therefore, we expect that in the near-fields the problem areas listed above will result in stray-light that is localized near the edges of the mask.

Based on this localization hypothesis, the total edge perimeter stands out as a good rule-of-thumb measure for predicting the level of stray-light in a given mask design. The edge perimeters from a few proposed masks are shown in

Table 2.1. The key finding is that the Barcode mask, while attractive from a simulation standpoint, may perform poorly due to its order of magnitude larger edge perimeter than any other mask. In order to create a working TPF-C

Mask Type	Perimeter (approx.)
Spergel Kasdin (1 opening)	0.14m
Spergel Kasdin (6 opening)	0.74m
Concentric Ring (20 rings)	0.3m
Star (20 point)	0.4m
Barcode	2×3m

Table 2.1: Approximate edge perimeters for 4×6cm masks. Stray-light edge effects are proportionate to the edge perimeter.

telescope we must track down the specific stray-light sources. To do this we turn to rigorous electromagnetic simulation and the specific methods that we use are presented in the next chapter.

Chapter 3

SIMULATION METHODS

3.1 The FDTD Method

The high contrast needed for exo-planet imaging requires detailed modeling of all physical effects present in a mask structure. The thin, perfectly absorbing mask model does not properly account for polarization, real materials, and edge scattering. There are many different simulation methods available for modeling light/structure interactions; however, the finite-difference time-domain (FDTD) method stands out for a few reasons.

1. The finite propagation speed of light decouples the field unknowns so that orders of magnitude larger structures can be simulated than with many frequency domain methods.

2. The time domain solution facilitates a qualitative understanding of the wave/structure interactions.

3. Since the FDTD method directly solves Maxwell's equations it can model many varied materials, such as highly lossy and dispersive materials, in a straight-forward manner.

The FDTD method directly solves a discretized version of Maxwell's curl equations (Ampere's and Faraday's Laws) by time-stepping the fields through a grid in space (Fig. 3.1). Each cell in the grid stores the current values of the $\vec{E}$ and $\vec{H}$ fields and also possesses material attributes that influence the way light travels through the cell. The fields are updated using a leap-frog algorithm wherein the E fields are updated based on the neighboring H fields, and then

(a) TE Grid.   (b) TM Grid.
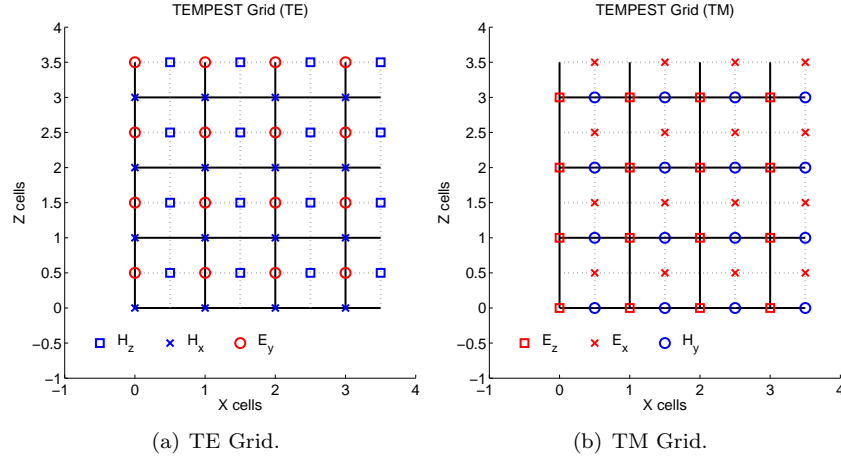
Figure 3.1: The spatial grids used by TEMPEST (the Berkeley TCAD group's FDTD simulator) for the two polarizations of a 2D simulation.

the H fields are updated based on the neighboring E fields. By repeating this process a steady-state solution can be achieved.

The updating equations are derived from Maxwell's equations using central difference approximations for the spatial and temporal derivatives leading to a scheme that is second order accurate in both space and time. Numerical errors (to be discussed later) are inversely proportional to the cell density squared[6]. Therefore error can be rapidly reduced by using finer grids; however, memory and computation time limit the effectiveness of this error mitigation scheme. Typically 20 cells per wavelength (in the most optically dense material) are adequate and are used in this work. The grid is terminated by an appropriate choice of boundary condition (BC). The two BC's used in this work are the periodic BC and Perfectly Matched Layers (PML). Periodic BC's wrap the fields from one edge of the grid around to the opposite edge effectively repeating the simulated geometry. PML are a type of material that absorbs waves without producing reflections thereby simulating a grid extending off into free-space.

The above capabilities have been implemented at U. C. Berkeley in a simulator called TEMPEST (used for the work in this report). Over the past 10 years TEMPEST has been used for analysis of problems in photo-lithography. TEMPEST is well within the accuracy requirements for lithography simulations; however, FDTD algorithms are typically only 0.1% to 0.01% accurate therefore

they do not have the accuracy required for full coronagraph mask simulation. In order to accurately model a coronagraph mask we combine the results of the Integrated Telescope Model and TEMPEST. First, the ITM is used to calculate the ideal fields transmitted by the ideal mask. Second, TEMPEST is used to compute the differences between realistic mask transmission and ideal mask transmission. Finally, these difference fields are used to correct the solution from the ITM. The difference fields are low intensity and only exist over small portions of the mask (near the edges) so they represent a very small correction to the mask transmission function. Thus, we expect that TEMPEST is well within the accuracy requirements for computing the difference fields (the final determination awaits full system simulation by the ITM). However, we must ensure that numerical effects do not hide the physical effects that we seek, so in the next section we discuss our efforts to characterize the primary numerical concerns in TEMPEST.

3.2   Numerical Effects

To ensure that the physical effects we study are not numerical artifacts we ran a series of simulations to characterize the three dominant sources of numerical error: numerical dispersion, source haze, and PML reflections.

The primary error, called numerical dispersion, is a type of phase error caused by discretizing the simulated geometry. It refers to the fact that a wave moving through the FDTD grid does not move as fast as expected resulting in a phase error. Additionally, these phase errors depend on the angle of propagation through the grid.

The second error, source haze, is another manifestation of numerical dispersion. In order to create a plane wave in TEMPEST electric and magnetic source fields are added to every cell in the source region. These fields are phased so that they interfere correctly in the direction of propagation; however, due to numerical dispersion these waves do not quite interfere correctly at all angles, leading to small, unintended waves propagating in odd directions. The last problem, PML reflections, refers to the fact that PML is not perfect and small reflections still arise.

To check all three effects we only needed to run one set of simulations. We placed a plane wave source in the middle of an empty simulation box (with PML on the top and bottom to absorb the outgoing waves) and varied the

angle of propagation (Fig. 3.2). To check the numerical dispersion we compared the phase along a vertical cut-line through the simulated data to the analytical solution for a propagating plane wave. We checked the PML reflections and source haze effects together by looking for any fields that leaked above the source plane.
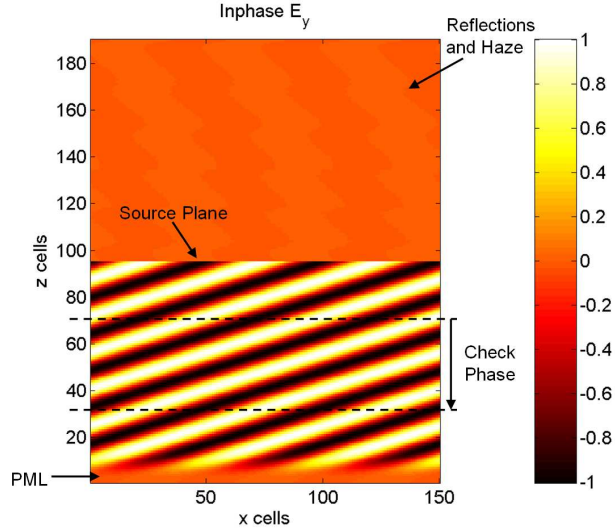
Figure 3.2: Field from one numerical dispersion, PML reflection, and source haze simulation.

The results of the numerical dispersion studies are shown in Fig. 3.3(a). We found that the error was relatively constant across the angles of interest and we measured the on-axis plane-wave to have a phase error of seven degrees after moving 50 wavelengths, or it was one cell short after moving 2650 cells. This means that the propagation distance had an error of 0.04%. Due to the relative uniformity and small amplitude of these errors, we applied a simple correction scheme to all the results in this paper - we corrected the phase of all the plane-waves as if they were on-axis. We did this by subtracting off the on-axis plane wave's phase error. This was judged to be sufficient since most of the plane-waves caught by the optical system are very close to on-axis.

The PML/source haze results (Fig. 3.3(b)) show that these concerns are orders of magnitude smaller than the physical effects under study. The difference field intensities from physical effects were of the order 10^{-3} whereas the PML/source haze intensity was of the order 10^{-6}. Therefore this source of error

was left untreated. We summarize these results in Table 3.1.

(a) Numerical dispersion.   (b) PML reflections and source haze.
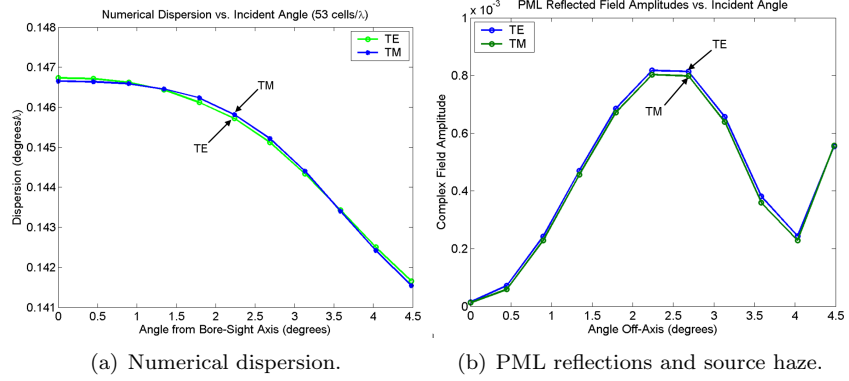
Figure 3.3: Magnitudes of numerical errors along different directions for a grid density of 53cells/λ.

In the next chapter we present the procedures used to uncover the physical effects that lead to the difference fields and the results of these simulation studies.

Area	Severity	Status	Bottom Line
Numerical Dispersion (ND)	**$7°$ short after 50 λ propagation (53cells/λ in air). This means the phase error is 0.04% of the theoretical distance traveled. Error is proportional to the cell size squared.**	**On-axis compensation complete. More accurate methods, e.g. higher order methods, harder to implement and on hold until needed.**	**Cut-line can be moved to within few wavelengths of aperture defining region to minimize numerical dispersion. Surface waves require special treatment (under investigation).**
PML Reflections/Source Haze	**$6.4*10^{-7}$ intensity. Four orders of magnitude below other ripples.**	**Not a problem, yet.**	**Different boundary conditions if necessary.**

Table 3.1: The status of the primary numerical concerns in TEMPEST. The severity of numerical dispersion is colored red because it dominates the list of numerical conerns; however, its bottom line is colored green because methods to counter numerical dispersion are availble (such as on-axis phase corrections and increased cell density). PML reflections/source haze are colored green in both severity and bottom line because these sources of error are smaller than the physical effects under study.

Chapter 4

STUDIES OF PHYSICAL EFFECTS

In this chapter we discuss the simulation studies of the physical phenomena present on a realistic mask structure. We start by describing the methods used to determine the difference fields and then move on to discuss the results of the specific studies.

4.1 Methods

In this section we describe the simulations we ran to uncover the non-ideal mask effects. For the initial analysis we modeled only one Barcode mask (upper left corner of Fig. 2.3). Additionally, we approximated this mask as a 2D periodic grating of infinite extent illuminated with a monochromatic, on-axis plane wave (propagation normal to the mask). All the results are normalized to this unit amplitude (one volt/meter) plane wave. This choice was made so that we could run fast simulations to discover unmodeled effects and their magnitudes. When running 2D simulations, the fields separate into two different polarizations with only one polarization present per simulation. When viewing fields in this paper (e.g. Fig. 3.2) the transverse electric (TE) polarization has $\vec{E}$ coming out of the page, whereas the transverse magnetic (TM) polarization has $\vec{H}$ coming out of the page.

The goal of the FDTD simulations is to bring the ideal model (as simulated by the ITM) into line with physical reality by adding difference fields as small

perturbations to the ideal mask transmission function. The specific process we use to compute the difference fields is as follows (Fig. 4.1):

1. Using TEMPEST we strike the mask with an on-axis plane-wave and propagate the light to an output plane below the mask.

2. Next, we take the complex field on the output plane into Matlab where we analytically propagate it back (without the mask) to the location of the top of the mask (aperture defining region).

3. Finally, still in Matlab, we take the intensity of the back-propagated TEM-PEST data and subtract off the intensity of the ideal field to obtain the intensity of the difference field.

This difference of intensities methods (the last step) was chosen to isolate the effects of amplitude mismatches between the ideal and TEMPEST data sets, with phase mismatches slated for future investigation.

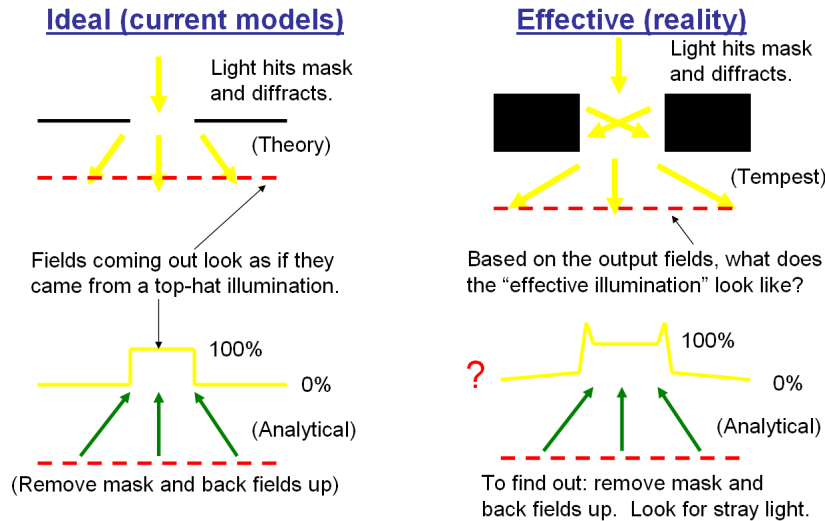Figure 4.1: The process for comparing the ideal and realistic fields to obtain the difference fields.

Even though a mask opening is set to one physical size, electro-magnetically it looks larger or smaller, meaning more or less light gets through than designed. This is caused by a number of effects, such as light penetrating into the material leading to leakage through the edges, light reflecting off the material, and the

material absorbing light. The opening's electromagnetic size (effective area) is dependent on polarization, mask material, sidewall geometry, and wavelength. Masks must be designed based on effective area and careful characterization of each opening must be performed to measure this area. In order to determine this area, we take the data from a simulated opening, subtract off the ideal field, and look at the differences. By varying the width of the ideal we can find the ideal that produces the smallest differences. The width of this ideal tells us the effective area. When examining the difference fields we look at two metrics: the magnitude of the on-axis transmitted wave relative to the ideal on-axis wave (simply the duty cycle of the grating) and the sum of the squared errors between all the simulated data (not just the on-axis wave) and the ideal. This leads to two different effective areas. The on-axis effective area is useful because it relates back to the analytical properties of the ideal model and the large F-number of the system means that most waves important to the system are very close to on-axis so they thus will perform in a similar manner to the on-axis wave. The sum of squared errors (SSE) effective area is useful because it indicates when off-axis waves differ from the ideal (in addition to the on-axis wave). We will carefully point out which effective area we are using when discussing the results.

When looking at the difference fields presented in the results section, it is important to note that we do not use all of the data produced by the simulator. Since the F-number of the TPF system is large only the plane waves very close to on-axis are caught by the system therefore, for the purposes of the pupil-plane mask analysis, the off-axis plane waves are excess data and are discarded. In effect, we low-pass filter the data (Fig. 4.2).

In the next section we present the results of simulations crafted to investigate the problematic physical effects of a pupil plane mask.

4.2 Results

In this section we summarize the results of the simulation studies of various physical effects. We take special care to layout the exact parameters and assumptions used in each set of simulations.
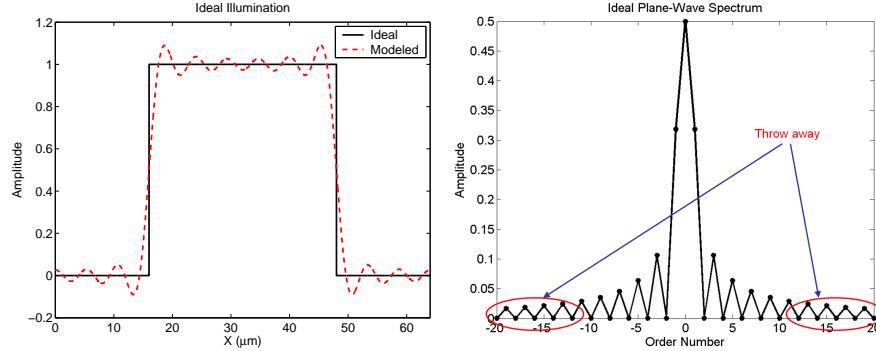
(a) The original ideal and the filtered ideal (ideal as modeled).

(b) The plane wave spectrum of the ideal and the filtered terms.

Figure 4.2: The ideal and the simulation data are filtered to remove the high-angle plane waves that are not caught by the optical system.

4.2.1 Sidewall Geometry

In the first set of simulations we checked the effects of sidewall geometry. We ran Chrome grating masks with three different sidewall geometries (Fig. 4.3): a thin mask consisting of 200nm of material, a thick straight edged mask consisting of 5.67μm of material, and an undercut mask consisting of 5.67μm of material with an undercut angle of $35.3°$ (the simulation parameters are summarized in Table 4.1). The thin mask is expected to be too flimsy to survive launch; however, it was included as an example of a mask that should perform very close to ideally.

From the difference fields (Fig. 4.4) it is apparent that the thin and undercut masks perform very closely to the ideal while the straight mask performs more than an order of magnitude worse than the undercut mask. The SSE effective areas (Table 4.2) also varied widely. By looking at the instantaneous fields pouring through the mask it was obvious that the straight mask suffered from heavy sidewall reflections that are not accounted for in the ideal model.

Since the undercut mask performed the best we decided to take a closer look at the effects of varying the undercut angle. J. Kasdin indicated that the undercut angle on the Princeton testbed masks was likely to be very small, so T. Shih ran simulations of $5.67\mu m$ thick Chrome masks with undercut angles of $2°$, $5°$, $10°$, and $18°$ (other simulation parameters are as indicated in Table 4.1). The results are plotted in fig. 4.5 (the straight-edge, $0°$, results are plotted for
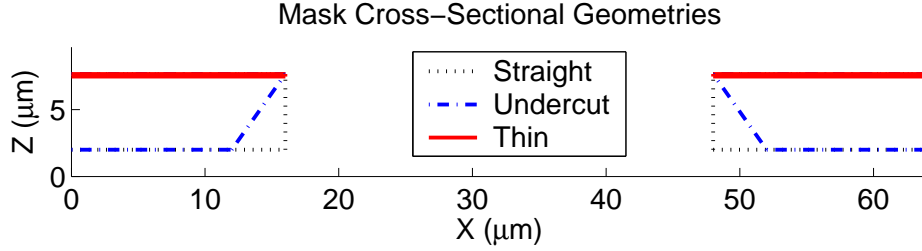
Figure 4.3: The three simulated cross-sections.

Parameter	Value
Wavelength	500nm
Material	Chrome ($n = 2.609 + j \times 4.455$)
Thickness	200nm and 5.67μm
Undercut Angle	$0°$ and $35.3°$
Mask Period	64μm
Mask Duty Cycle	50%
Polarization	TE and TM

Table 4.1: The simulation parameters used in the initial sidewall geometry study of thin, vertical, and undercut sidewalls.

reference).

As expected, as the undercut angle increased the opening in the mask grew (Table 4.3). In the TE case, for small angles the effective area of the opening was less than the physical area due to the loss of light to the mask material through sidewall interactions. Above $10°$ the effective area was actually larger than the physical area, due to corner leakage. The case was a little different for the TM polarization, where the effective area was always smaller than the physical area,

	$\Delta\text{Opening}_{TE}$	$\Delta\text{Opening}_{TM}$
Undercut	+0.15 λ	-0.11 λ
Straight	-1.21 λ	-2.60 λ
Thin	-0.11 λ	-0.11 λ

Table 4.2: The differences between the SSE effective area and the designed width of one opening of a 64μm period Chrome grating with varied sidewall geometry and thickness ($\lambda = 500nm$).

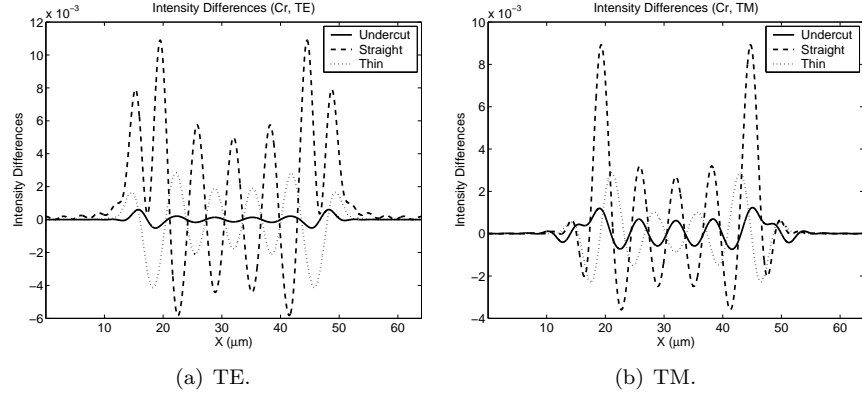(a) TE.   (b) TM.

Figure 4.4: The difference field intensities from the initial sidewall geometry study.

Undercut Angle	$\Delta\text{Opening}_{TE}$	$\Delta\text{Opening}_{TM}$
$0°$	-1.21 λ	-2.60 λ
$2°$	-0.87 λ	-2.19 λ
$5°$	-0.42 λ	-1.70 λ
$10°$	0.00 λ	-0.98 λ
$18°$	0.15 λ	-0.11 λ

Table 4.3: Change in opening size (from the physically designed size) for Chrome masks with various undercuts ($\lambda = 500nm$).

due to sidewall interactions and lossy surface waves (discussed in Sect. 4.2.2) attenuating the light. Interestingly, between $5°$ and $10°$ the magnitude of the difference fields dropped significantly, indicating that there may be a maximum angle for efficient generation of surface waves, beyond which the surface waves are barely excited.

4.2.2 Opening Size and Polarization

The second set of studies checked the performance of various opening sizes and polarizations (based on previous work done at JPL[7]). For these tests we ran a number of 0.6λ thick, 30λ period perfect electrical conductor (PEC) gratings (simulation parameters can be found in Table 4.4). Each grating had a different duty cycle, starting with a completely closed grating (slab of PEC) up to a completely open grating (entirely free-space). We checked the on-axis transmission
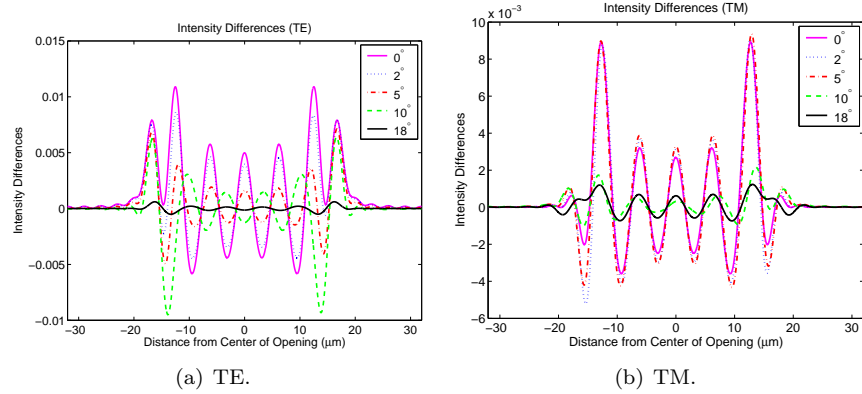
(a) TE.   (b) TM.

Figure 4.5: The difference field intensities for different undercut angles. The 18° undercut is represented by the solid line with the smallest amplitude ripples and the 0° undercut if represented by the solid line with the largest amplitude ripples. The small asymmetries in the fields are due to small asymmetries in the layout of the simulations.

amplitude and phase against theory and found marked differences (Fig. 4.6). Very small openings exhibited much lower transmission than expected, and the transmission was polarization dependent. The phase was strongly affected in small openings, and the sign of the phase change depended on the polarization, indicating that compensation for a mask with small openings may be challenging.

Parameter	Value
Wavelength	500nm
Material	Perfect Electrical Conductor
Thickness	300nm
Undercut Angle	0°
Mask Period	15μm
Mask Duty Cycle	0% to 100%
Polarization	TE and TM

Table 4.4: The simulation parameters used in the initial polarization/duty cycle study of PEC gratings.

Since less light went through the mask than expected T. Shih zoomed in on the middle portion of the transmission magnitude plot (Fig. 4.6(a)), ran more simulations with a finer variation of the duty cycle, and fit a curve to the data.
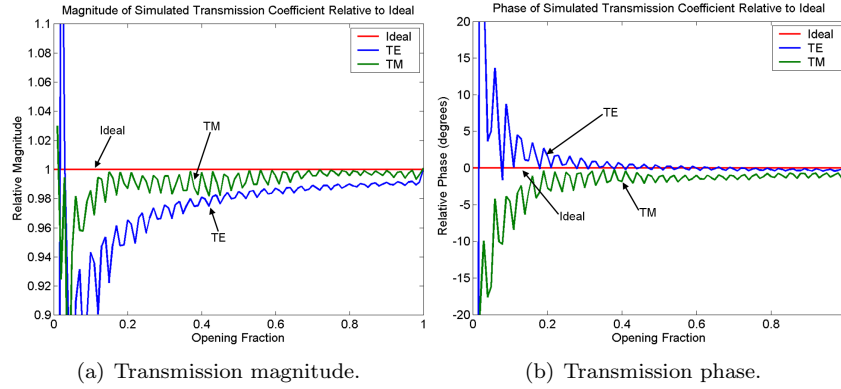
(a) Transmission magnitude.   (b) Transmission phase.

Figure 4.6: The on-axis transmission properties vs. duty cycle for a 0.6λ thick, PEC grating with a period of 30λ. All values have been normalized to the ideal.

The ideal model predicts that the on-axis transmission equals the grating's duty cycle, i.e. $T = W/P$, where W is the physical width of an opening and P is the period of the grating. He assumed that the reduction in transmission could be modeled simply as a reduction in opening size and derived the opening reduction curve (ORC):

$$T = \frac{W - L}{P} \tag{4.1}$$

where L is a small correction factor to the width to account for electromagnetic effects. He found this curve fit quite well and it computed opening corrections of $L_{TE} = 1.47\lambda$ and $L_{TM} = 1.03\lambda$, for PEC gratings, that are approximately independent of the size of the opening! Thus, the ORC predicts that a mask will perform as intended as long as we increase the openings slightly; however, the fact that these corrections are strongly polarization and wavelength dependent (the anticipated TPF-C wavelength range is 0.5μm – 0.8μm) may rule out such a simple compensation technique.

In addition to computing the ORC, T. Shih also looked for edge-to-edge cross-talk, i.e. fields that bounce off one side of the mask opening and then interact with the other side before exiting the mask. This affect manifests itself as ripples in the transmission amplitude as the duty cycle of the mask is changed (Fig. 4.6(a)). It was at this point that we uncovered a bug in TEMPEST, namely the PEC does not work correctly (all fields are set to zero in the PEC so that at some boundaries normal field components are set to zero in addition to the tangential field components). Switching to Chrome masks (with the simulation

parameters shown in Table 4.5), T. Shih concluded that the cross-talk was minimal because the ORC's for both vertical sidewalls and undercut sidewalls were smooth (Fig. 4.7). We next looked for explanations for the polarization imbalance.

Parameter	Value
Wavelength	500nm
Material	Chrome ($n = 2.609 + j \times 4.455$)
Thickness	5.67μm
Undercut Angle	$0°$ and $35.3°$
Mask Period	64μm
Mask Duty Cycle	50% to 56%
Polarization	TE and TM

Table 4.5: The simulation parameters used in the edge-to-edge cross-talk simulations.

(a) TE.   (b) TM.
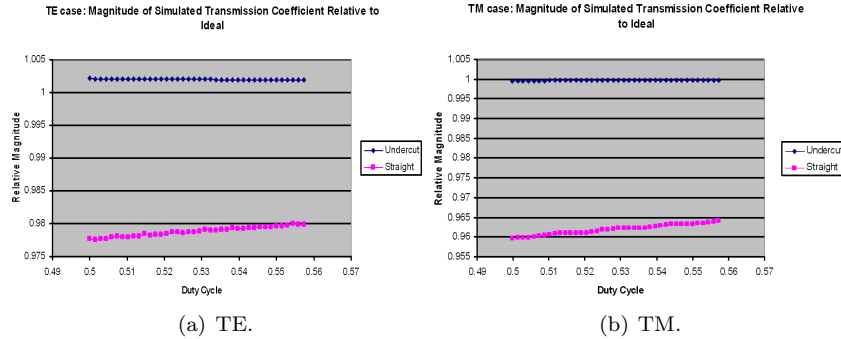
Figure 4.7: The opening reduction curves that indicate little cross-talk between the two edges of an opening in a Chrome mask. Note that the ripples, indicative of cross-talk, are very small.

The transmission imbalance due to polarization can be, at least in part, explained by surface waves. If we look at the instantaneous fields running around the mask we note surface waves for the TM polarization (Fig. 4.8) but not the TE polarization. The surface waves are due to surface charge oscillations excited by the incident light as it passes the corners of the mask. These surface waves are called surface plasmon polaritons[8] (SPP's). These waves are electromagnetic waves coupled to charge oscillations that exist only at an interface between a metal and a dielectric (more generally the "metal" need only be a material

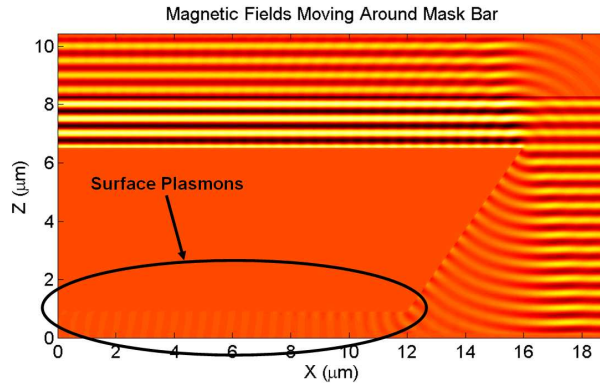Figure 4.8: Instantaneous magnetic fields propagating through an Aluminum grating. Notice the surface waves on the bottom of the bar decay rapidly away from the opening.

with a negative permittivity). Light falling on the mask can couple into surface plasmons through corners and surface roughness, created during manufacturing, and can radiate back into free-space when it hits more roughness or a corner (such as the corners on the bottom of the mask). Since these waves can travel up to a few microns (depending on the material) they are a candidate for more stray light in addition to energy loss through heating.

At Berkeley we have begun investigations into simulating plasmons. Specifically, we have experimented with a number of ways to create surface plasmons in TEMPEST (Fig. 4.9). Surface plasmons have received increasing attention in recent years due to their potential uses in spectroscopy, biological tracers, and waveguides. We feel that they are an important effect to model in TPF-C masks and plan to continue our efforts to characterize SPP's.

4.2.3 Materials

In the last set of physical studies we investigated the effects of different materials. Initially, we assumed the mask would be made of metal but after the group at Princeton looked into manufacturing a mask for their testbed it became apparent that Silicon is a strong candidate due to the manufacturing capabilities available from the semiconductor industry.

We first tested three metals at $\lambda = 500nm$: Nickel ($n_{Ni} = 1.6758 + j2.956$), Aluminum ($n_{Al} = 0.769 + j6.08$), and Chrome ($n_{Cr} = 2.609 + j4.455$)[9]. We ran

(a) Layout of a surface plasmon simula-
tion.

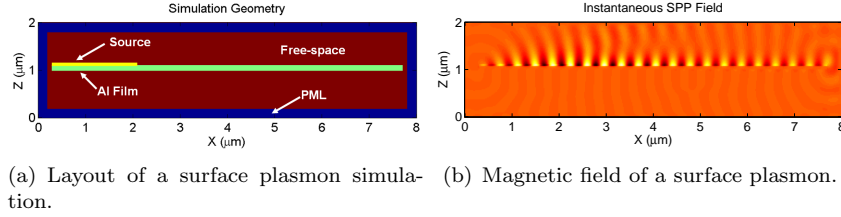(b) Magnetic field of a surface plasmon.

Figure 4.9: A simulation of a surface plasmon on a thin Aluminum film ($\lambda_0 = 400nm$). The plasmon is excited by a series of electric dipoles placed along the upper surface of the film and phased to reproduce the surface plasmon wavelength.

the same simulation for each material (the parameters are listed in Table 4.6) and tried both TE and TM polarizations. Table 4.7 demonstrates that not only does the effective area depend on the material but the polarization determines the sign of the change. Furthermore, the difference fields (Fig. 4.10(a)) differ depending on material and polarization. The Aluminum goes from being the best performer in the TE case to the worst in the TM case! For the TE polarization, we expect that the increase in transmission is due to light leaking through the mask's corners. For the TM polarization, we anticipate the decrease in transmission is due to surface currents putting energy into the metal. Additionally, the large ripples in the Aluminum's difference field may be explained by surface currents radiating at the mask corners.

Parameter	Value
Wavelength	500nm
Material	Nickel ($n = 1.6758 + j \times 2.956$)
	Chrome ($n = 2.609 + j \times 4.455$)
	Aluminum ($n = 0.769 + j \times 6.08$)
Thickness	$5.67\mu m$
Undercut Angle	$35.3°$
Mask Period	$64\mu m$
Mask Duty Cycle	50%
Polarization	TE and TM

Table 4.6: The simulation parameters used in the study of different mask metals.

We next turned to Silicon, the material used in the current generation of Princeton testbed masks. The biggest problem with Silicon is that, if not doped

	$\Delta\text{Opening}_{TE}$	$\Delta\text{Opening}_{TM}$
Al	$+0.15\lambda$	-0.19λ
Cr	$+0.15\lambda$	-0.11λ
Ni	$+0.19\lambda$	-0.08λ

Table 4.7: The difference between the designed width and the SSE effective area of one opening of a 64μm period, undercut grating comprised of different metals. The opening gets larger or smaller depending on the material and the polarization.
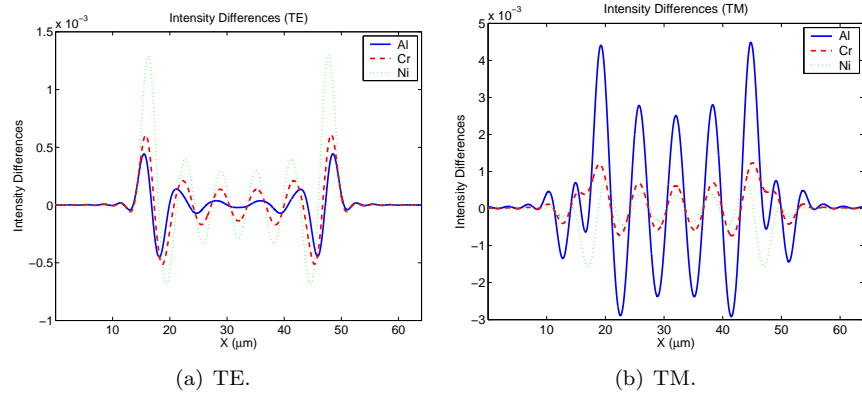

(a) TE.   (b) TM.

Figure 4.10: The difference field intensities for various mask metals.

properly, it can be very leaky.

Looking at the literature[10][11][12][13] on the absorption coefficient of Silicon we found that all the papers agree on the general trend, that absorption increases with increased levels of doping, but the exact values do not always agree. Specifically, the different sets of experimental data in the infra-red region agree with each other but the data in the optical region do not agree (Fig. 4.11). The disagreement may be due to different methods of preparing the Si samples and different measurement techniques. The most important point taken from these papers is that n-type dopants more strongly affect the absorption coefficient than p-type dopants. Therefore, future masks should be made with n-type Si.

The current generation of testbed masks was made out of $50\mu m$ thick p-type doped Silicon with doping levels between $1.3 \times 10^{15}/cm^{-3}$ and $1.3 \times 10^{16}/cm^{-3}$ (the manufacturer measured the resistivity of the wafers to be between 1 and
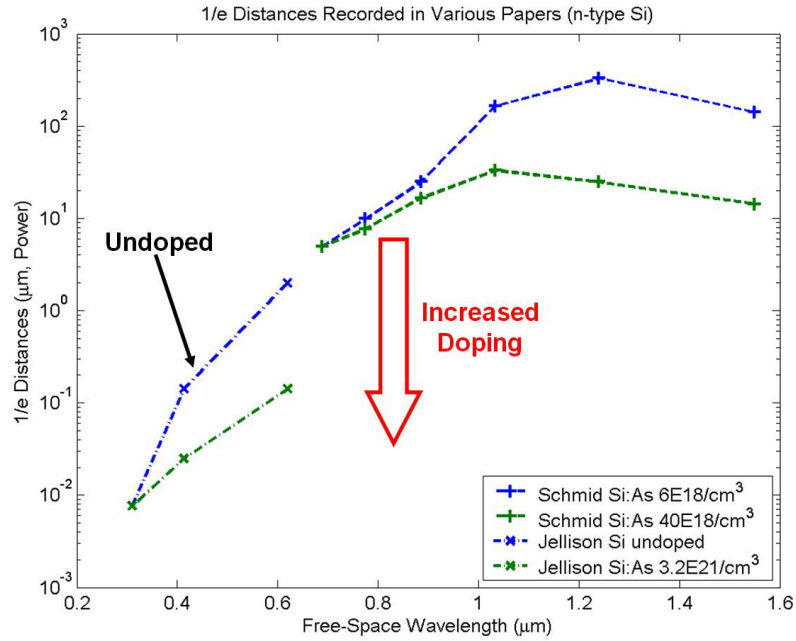
(a) N-type Si.
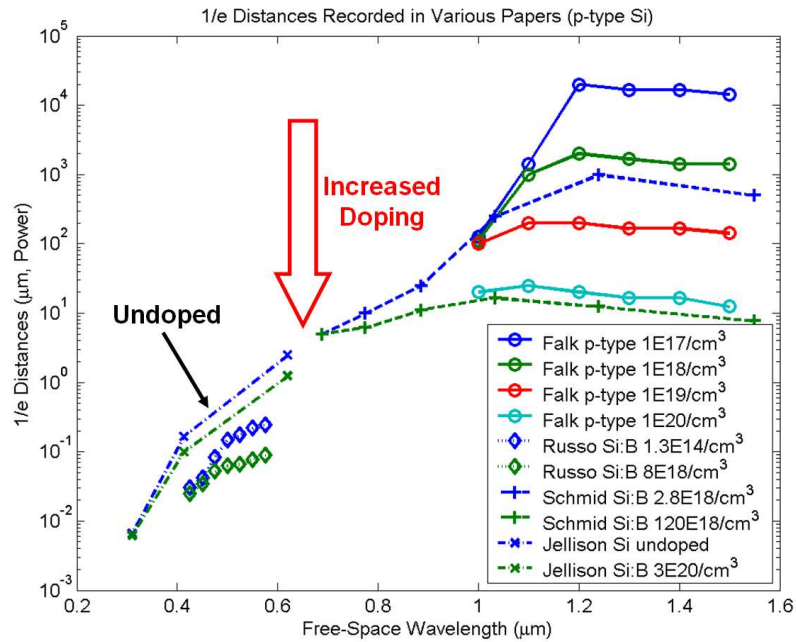
(b) P-type Si.

Figure 4.11: Experimental values of the skin depth of Silicon in the optical and infra-red regimes (from the literature).

10 Ω-cm). In order for the light that penetrates into the mask to decay to the 10^{-10} level in intensity after 50μm of Silicon the skin depth (1/e distance) must be less than 2.17μm. The light-source used on the testbed has a wavelength of 632nm, therefore depending on which absorption measurements you believe, this puts the skin depth of the testbed mask at either 2.321μm or 0.231μm (shown in greater detail in Fig. 4.12). The former will not attenuate to the appropriate level whereas the latter will.

A possible solution for a leaky mask is to coat the top of the mask with a thin layer of metal (dark Chrome is typically used by the IC industry for photomasks). We investigated the effects of coating a leaky Si mask by simulating two different 8μm thick Si masks (skin depth of 2.321μm, equivalent to extinction coefficient of $K = 0.0216$): one with a $10°$ undercut and the other with a $20°$ undercut. We simulated the masks both with and without a $200nm$ layer of Chrome on top. As before, the masks were approximated as gratings with a 64μm period and a 50% duty cycle. We used a 630nm wavelength to match the testbed's light source (the simulation parameters are summarized in Table 4.8).

Parameter	Value
Wavelength	630nm
Material	Silicon ($n = 3.88 + j \times 0.0216$) with and without 200nm Chrome coating
Thickness	8μm
Undercut Angle	$10°$ and $20°$
Mask Period	64μm
Mask Duty Cycle	50%
Polarization	TE and TM

Table 4.8: The simulation parameters used in the study of Silicon undercuts and coatings.

The coating made a large difference. As expected, the uncoated Silicon leaked causing the opening to appear larger than designed but coating the masks caused the change in opening size to drop from about one wavelength down to less than a fifth of a wavelength, $10°$ undercut, or three hundredths of a wavelength, $20°$ undercut (Table 4.9). The data also indicates that when comparing coated masks with different undercut angles the steeper undercut will perform better. From this we deduce the corner leakage is no longer a concern due to the coating and the sidewall interaction is reduced by a steeper undercut (Fig. 4.13).
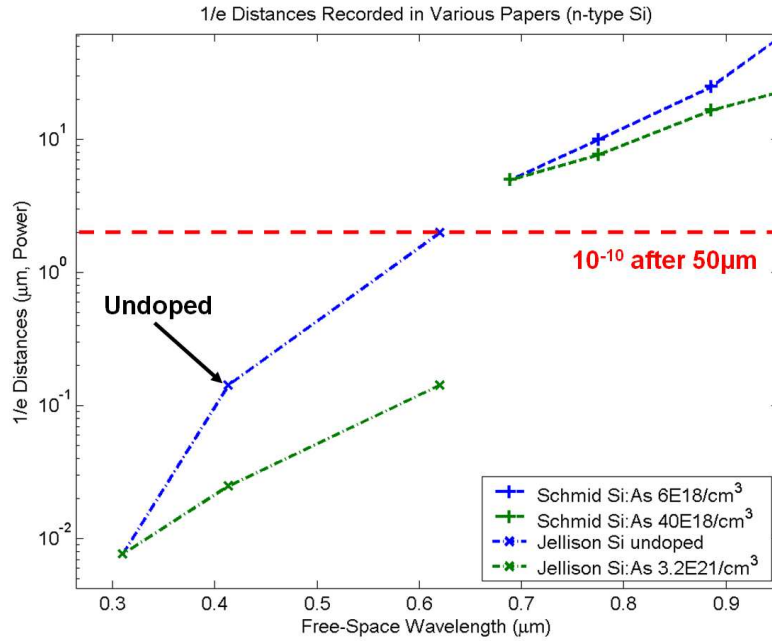
(a) N-type Si.
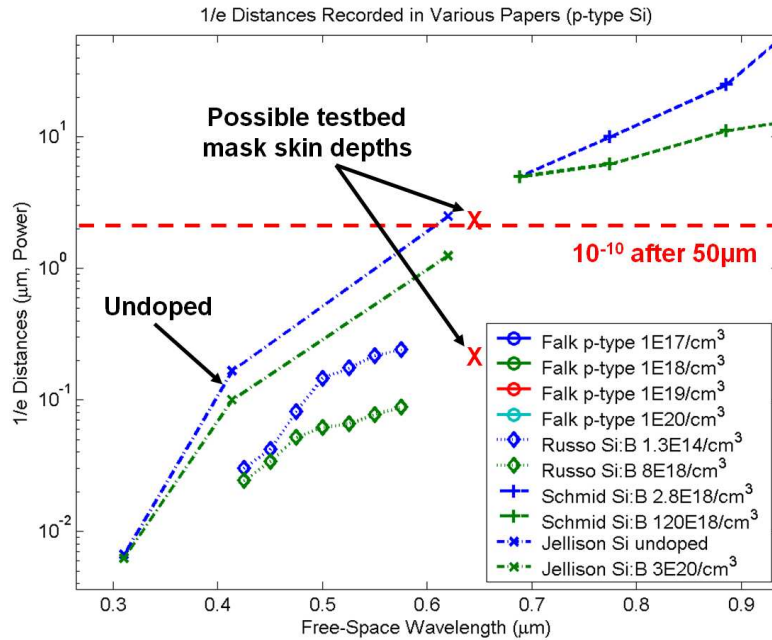
(b) P-type Si.

Figure 4.12: Experimental values of the skin depth of Silicon in the optical regime (from the literature) and the possible skin depths for the current testbed mask.

Mask Layout	ΔOpening$_{TE}$	ΔOpening$_{TM}$
$10°$ uncoated	$+1.037\ \lambda$	$+0.993\ \lambda$
$10°$ coated	$-0.055\ \lambda$	$-0.183\ \lambda$
$20°$ uncoated	$+1.008\ \lambda$	$+1.040\ \lambda$
$20°$ coated	$+0.030\ \lambda$	$+0.003\ \lambda$

Table 4.9: The on-axis effective area of one opening of a 64μm period, 8μm thick, undercut Silicon grating both with and without a 200nm Chrome coating on top.
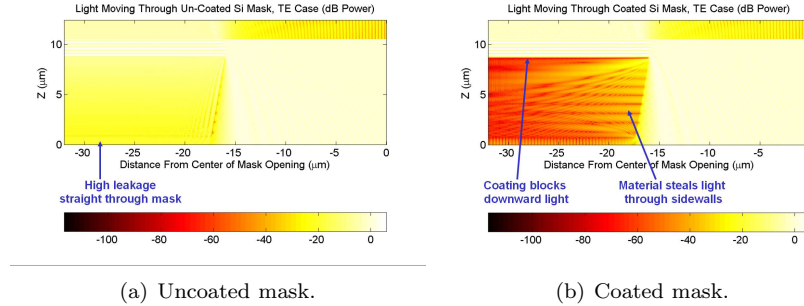

(a) Uncoated mask.   (b) Coated mask.

Figure 4.13: The fields (in dB intensity) moving through a $8\mu m$ thick, $10°$ undercut Silicon mask.

As a side note, the difference between polarizations cannot be explained by surface plasmons on the Silicon because they are not supported on Silicon with the refractive indices used in these studies (N=3.88 and K=0.0216).

We also investigated $50\mu m$ thick Silicon masks (to better represent the current generation of testbed masks which are minimally $50\mu m$ thick) with a higher doping level than before (K=0.216, corresponding to a skin depth of $0.2321\mu m$). We ran simulations of a vertical sidewall mask and $20°$ undercut masks with and without the same Chrome coating layer. Due to the thickness of the masks and the steep undercut the period of the grating had to be increased to $96\mu m$ ($48\mu m$ wide bars) so that the sidewalls did not meet, reducing the thickness of the bars (Table 4.10). In these simulations the coating did not have nearly as large an effect as before (Table 4.11) for two reasons. One, the Silicon was more attenuating so less light leaked straight through the mask. Two, the period of the mask was larger so the corner effects accounted for a smaller percentage of the total energy passing through the opening.

Parameter	Value
Wavelength	630nm
Material	Silicon ($n = 3.88 + j \times 0.216$) with and without Chrome coating
Thickness	50μm
Undercut Angle	$0°$ and $20°$
Mask Period	96μm
Mask Duty Cycle	50%
Polarization	TE and TM

Table 4.10: The simulation parameters used in the study of 50μm Silicon masks.

Mask Layout	$\Delta\text{Opening}_{TE}$	$\Delta\text{Opening}_{TM}$
$0°$ uncoated	-3.85 λ	-4.09 λ
$20°$ uncoated	+0.063 λ	-0.064 λ
$20°$ coated	+0.040 λ	-0.058 λ

Table 4.11: The on-axis effective area of one opening of a $96\mu m$ period, $50\mu m$ thick Silicon grating both with and without a 200nm Chrome coating on top.

The most important observation from these studies was that sidewall undercut angle again played a very important role. The need for undercut sidewalls is especially strong for high refractive index materials, such as Si, because the large N pulls light into the material. The vertical sidewall opening was about four wavelengths narrower than designed whereas the $20°$ undercut opening deviated only a few hundredths of a wavelength from the designed width.

All of the results of this section are summarized in Table 4.12.

Area of Concern	Severity	Future Work	Expected Bottom Line
Materials	Lossy metals: •Switching metals changes opening size by ~0.1 wavelengths. •Good under TE (minimize leakage). •Bad under TM (surface waves). •Highly dependent on wavelength! Si: •Leaky masks change opening size by multiple wavelengths. •Heavily doped and/or coated masks change opening size by ~0.05 of a wavelength.	Different materials will be added as they come into consideration for possible use in the testbed masks.	Proper choice of material can balance leakage and surface waves at *one wavelength*. Cr is good balance at 500nm. Properly doped and/or coated Si will perform at least as well as a metal.
Edge geometry	Sidewall interactions are paramount! •Vertical-edge is 20x worse than 35.3° undercut in intensity. •Vertical edges can change opening size by over a wavelength! •Undercut edges can change opening size by about one tenth of a wavelength.	Farther investigation of the dependence of sidewall interactions and surface plasmons on undercut angle and corner geometry.	Undercut looks best. What is adequate depends on end-to-end effects
Polarization	Material choices are important! >5% Magnitude and >10° difference between TE and TM for small openings (sub 6 λ). TE causes openings to increase by 0.1-0.2 wavelengths whereas TM closes the openings by similar amounts.	Surface plasmons may account for polarization imbalance. Surface plasmons are under investigation.	Problem for small openings! Barcode openings may be large enough to mitigate effects, although surface waves may cause problems.
Edge-to-Edge Cross Talk	Small.	On hold unless full system simulation indicates that it is a concern.	Smaller than surface waves and polarization effects.

Table 4.12: The severity and status of the major physical concerns. Undercut angle and material are the most important choices in the mask design. The severity of the materials, edge geometry, and polarization concerns are colored red to indicate that they top the list of concerns. Cross talk has been shown to be a very small problem and consequently has been colored green. The bottom lines for materials and polarization are colored orange to indicate that solutions will be difficult to implement due to dependencies (such as wavelength and opening size); however, these difficulties are not insurmountable and the work in this paper has indicated directions to explore for solutions. The bottom line for edge geometry has been colored green because undercutting solves this problem and is an implementable solution. The bottom line for cross talk is also colored green because the problem is very small compared to other issues.

Chapter 5

CONCLUSIONS

In this report, we looked into the primary physical sources of stray-light on pupil plane masks and sources of numerical error in the FDTD method using 2D monochromatic simulations. On the numerical side we investigated phase errors in the form of numerical dispersion and the noise associated with source haze and PML reflections. On the physical side we looked at real metals, thick masks, sidewall geometry, and polarization and how these effects caused the light passing through the mask to differ from the predictions of ideal theory.

Turning to the numerical issues, using $53 \text{cells}/\lambda$ we showed the phase error (numerical dispersion) to be 0.04% for light moving through free-space. This was farther reduced to 0.014% (half a degree after $50\mu\text{m}$ at $\lambda = 500\text{nm}$) by applying an on-axis phase correction for all the waves contributing to the difference fields. The PML and source haze noise was shown to be three orders of magnitude (in intensity) below the physical effects under study and was left untreated. A final verdict on whether or not these accuracy levels meet the TPF-C requirements awaits full system simulation by the ITM.

On the physical side we showed that the undercut angle and the mask material are the most important implementation choices. Changing the undercut angle from $0°$ to $20°$ reduced the change in opening size from $1\text{-}4\lambda$ to $\lambda/5\text{-}\lambda/20$. Different metals can change the mask opening size by $\lambda/10$. Silicon is a good choice for a mask material; however, it must be heavily doped or coated with metal to prevent leakage. Coating works quite well with only 200nm of Chrome dropping the change in opening size from λ down to $\lambda/5$ and below. Polarization has large consequences on the mask opening sizes. Metal masks have the problem that one polarization causes the openings to narrow by $\lambda/10$ while the

other polarization causes the openings to widen by the same amount making compensation difficult. A nice property of Silicon masks is that the change in opening size has the same sign under both polarizations, leaving the door open for compensation in the design. However, the opening size changes are wavelength dependent so compensation will not be an easy task.

An outstanding question is whether or not the stray-light caused by the effects studied in this report is localized to the edges of the mask. The data does not definitely confirm nor discredit this localization hypothesis. Difference fields such as those shown in Fig. 4.4(a) indicate strong differences across the entire opening whereas the difference fields shown in Fig. 4.10(a) show localization to the edges. Preliminary looks at data with the phase taken into account and no low-pass filtering show the stray-light to be localized near the edges. We anticipate mask corners to be the only remaining significant physical source of stray-light to be analyzed because there is very little edge-to-edge cross talk, leakage can be adequately addressed through material choice and/or coating with thin metal layers, and sidewall interactions can be minimized through undercutting.

In the future we plan on extending the current studies to include off-axis plane waves, polychromatic light, and 3D simulation studies of cross-polarization effects. This work will be directed towards building libraries of responses for typical structures appearing on pupil-plane masks such as edges, points, grooves, and tool-marks. Additionally, we are in the process of integrating these results into Ball Aerospace's Integrated Telescope Model to obtain information about the difference fields' impact on the total system's performance.

Bibliography

[1] J. Kasdin, R. Vanderbei, D. Spergel, and M. Littman, "Extrasolar planet finding via optimal apodized-pupil and shaped-pupil coronagraphs," *The Astrophysical Journal* **582**, pp. 1147–1161, 2003.

[2] D. Ceperley, A. Neureuther, M. Lieber, J. Kasdin, and T.-M. Shih, "Vector scattering analysis of tpf coronagraph pupil masks," in *Stray Light in Optical Systems: Analysis, Measurement, and Suppression*, **5526B**, SPIE, Aug. 2004.

[3] D. Ceperley, A. Neureuther, M. Lieber, and J. Kasdin, "Characterizing edge generated stray light sources for tpf coronagraph pupil masks," in *Techniques and Instrumentation for Detection of Exo-Planets II*, SPIE, Aug. 2005.

[4] M. Lieber, A. Neureuther, D. Ceperley, J. Kasdin, and N. Ter-Gabrielyan, "Vector wavefront propagation modeling for the tpf coronagraph," in *SPIE Astron. Telescopes*, June 2004.

[5] Vanderbei, Kasdin, and Spergel, "Checkerboard mask coronagraphs for high-contrast imaging," *The Astrophysical Journal* **615**, pp. 555–561, Nov. 2004.

[6] A. Taflove and S. Hagness, *Computational Electrodynamics: The Finite Difference Time Domain Method*, Artech House, 2 ed., 2000.

[7] D. Hoppe and T. Cwik, "Full-wave effects in coronagraph masks," *TPF Science, Technology, and Design Expo* , Oct. 2002. http://planetquest1.jpl.nasa.gov/tpf/expo03/dsp_tpfAgendaDetail.cfm?id=a186.

[8] H. Raether, "Surface plasma oscillations and their applications," in *Physics of Thin Films*, G. Hass, M. Francombe, and R. Hoffman, eds., **9**, pp. 145–261, Academic Press, 1977.

[9] B. W. Smith, "Optical properties of thin films for duv and vuv microlithography," tech. rep., Rochester Institute of Technology, 2004. http://www.rit.edu/ 635dept5/thinfilms/thinfilms.htm.

[10] R. A. Falk, "Near ir absorption in heavily doped silicon - an empirical approach," in *Proceedings of the 26th ISTFA*, 2000.

[11] J. G. E. Jellison, F. A. Modine, C. W. White, R. F. Wood, and R. T. Young, "Optical properties of heavily doped silicon between 1.5 and 4.1 ev," *Physical Review Letters* **46**, pp. 1414–1417, May 1981.

[12] O. L. Russo, "Optical constants of silicon by unpolarized incident radiation," *Journal of the Electrochemical Society: Solid-State Science and Technology* , pp. 953–956, 1980.

[13] P. E. Schmid, "Optical absorption in heavily doped silicon," *Physical Review B* **23**, pp. 5531–5536, May 1981.